Available online at www.sciencedirect.com
SCIENCE DIRECT®
International Journal of Solids and Structures 43 (2006) 5886–5908
INTERNATIONAL JOURNAL OF SOLIDS and STRUCTURES
www.elsevier.com/locate/ijsolstr

Damage imaging of reinforced concrete structures using electromagnetic migration algorithm

Saeed Nojavan *, Fuh-Gwo Yuan *

North Carolina State University, Dept. of Mechanical and Aerospace Eng., Box 7921, Raleigh, NC 27695-7921, USA

Received 17 May 2005
Available online 24 October 2005

Abstract

Reconstructing damage geometry with computationally efficient algorithms is of primary importance in establishing a robust structural health monitoring system (SHMS). In this paper electromagnetic migration, a linearized imaging algorithm, is adopted to image the damages in reinforced concrete structures. This algorithm is formulated in time-domain for 3-D inhomogeneous isotropic and lossy structures. In order to reduce the computational cost and to examine the damage resolution of this imaging algorithm, different imaging conditions are introduced. Numerical simulations in 2-D transverse magnetic (TM) wave for a reinforced concrete slab with multiple damages are performed to test the effectiveness of the algorithm. All synthetic sensor data, incident field, and migration field are computed via a finite difference time-domain (FDTD) method. It is concluded that the proposed imaging algorithm is capable of efficiently identifying the damages geometries, is robust against measurement noise, and may be employed in a SHMS.

Keywords: Electromagnetic migration algorithm; Structural health monitoring; Damage imaging; Prestack; Poststack; Finite difference method

1. Introduction

The integrity of structures such as aircrafts, bridges and dams needs to be monitored to avoid unexpected failures. In order to ensure both safety and functionality of these structures and prevent their failures, it is crucial to continuously diagnose their condition and detect the presence, the location, and the extent of damages as they occur. Proper corrective actions can then be taken to temporarily mitigate the effects of such damages until structures can be repaired.

Periodic inspections or scheduled maintenance using conventional nondestructive inspection (NDI) techniques require extensive labor, cause downtime, and are expensive. Most inspection techniques such as conventional ultrasonic or eddy currents need a transducer to be scanned over each point of the structure

* Corresponding authors. Tel.: +1 919 515 5947; fax: +1 919 515 5934.
E-mail addresses: snojavan@yahoo.com (S. Nojavan), yuan@eos.ncsu.edu (F.-G. Yuan).

0020-7683/$ - see front matter
doi:10.1016/j.ijsolstr.2005.08.017

under inspection which is a time-consuming process. Moreover, for structural components that are hard to inspect, disassembly of the structure may be required (Krautkramer and Krautkramer, 1990; Bray and McBride, 1992).

The essence of structural health monitoring (SHM) technology is to develop autonomous built-in systems for the continuous real-time monitoring, inspection, and damage detection of structures with minimum labor involvement (Chang, 1997). The potential benefits from a SHMS are enormous such as real-time monitoring and reporting, saving in maintenance cost, reducing labor, downtime and human error, and improving safety and reliability. Typically, such a built-in diagnostic system, in addition to the structures to be monitored, would include two major components: a built-in network of sensors for collecting sensor measurements and damage identification software for interpretation of sensor measurements in terms of the physical condition of the structures. There are two types of diagnostic systems based on sensor functionality: passive sensing system without known inputs (sensor only) and active sensing system with known inputs (both sensors and actuators). A passive system uses sensors such as MEMS, fiber optics, accelerometers, and strain gages to measure changes in structures due to the change in environmental conditions in terms of loads, temperature, chemistry, etc. Along with sensors, an active system is also equipped with actuators to generate diagnostic (excitation) signals to interrogate the ''health'' status of the structures. A passive system is more adequate for monitoring the condition of the structures while an active system is more capable of detecting damage in the structures.

Generally, the excitation signal in an active SHMS can be mechanical or non-mechanical. Mechanical signals, such as acoustic, ultrasonic, and elastic waves, are those in which a mechanical medium (i.e. solid, fluid, or gas) is required for wave propagation. In contrast, non-mechanical waves, such as electromagnetic (EM) waves, can propagate in any medium including vacuum, thereby enabling non-contact diagnosis. It is worth mentioning that radio waves, microwaves, infrared light, visible light, ultraviolet light, X-rays, and γ -rays are different parts of the EM spectrum. However, hereafter, ''EM waves'' will imply the microwave region of the EM spectrum, generally between a few hundred MHz and a few hundred GHz (Bahr, 1995). It should be noted that various types of excitation signals with different waveforms may provide different degrees of sensitivities to a specific type of damage in a structure. In fact the sensor response from the selected excitation signal depends on the interaction between sensor/actuator and structure, the material properties of the structure (including the structure) through which the signal propagates, and the damage mechanisms.

Regarding the sensitivity of using mechanical and non-mechanical signals in detecting the damages, Lemistre and Balageas (2004) showed that low frequency EM wave signals (700 KHz) were more sensitive to damages generated by aggressions such as burning, lightning, and liquid ingress in carbon/epoxy composites; elastic wave signals (400 KHz) more sensitive to delaminations. Buyukozturk (1998) concluded that microwave technique was effective in locating and imaging subsurface defects and inclusions in concrete structures. However, microwave signals experienced high attenuation in moisture, and total reflection from metals which made it difficult to image areas beneath closely spaced rebars. On the other hand, in ultrasonic method, although the ultrasonic wave signals were not affected by the presence of reinforcements and moisture, they suffered high attenuation for the aggregate sizes comparable to the excitation wavelength due to aggregate scattering (Iyer et al., 2005). Zoghi (2000) and Liu and Bethesda (1998) also showed that the ultrasonic method may not be a good choice for NDI of thick, multilayered composite structures especially when composites are made of porous, coarse grained, low permittivity or low loss dielectric materials such as glass fiber composites, commonly used for ship-hall and masts in marine environments. The high attenuation of elastic waves in such materials dictates the application of relatively low excitation frequency in order to obtain the required penetration depth, thereby reducing image depth resolution. On the contrary, EM waves can penetrate deep inside these materials and interact with their inner structure without suffering from high attenuation. A reverse situation occurs with conductive materials (i.e. metals) or non-perfectly conductive materials (e.g. carbon/epoxy composites) where the high attenuation of EM waves forces the use of relatively low excitation frequency, leading to a poor depth resolution of the image. Considering the above arguments, it can be concluded that in order to identify all types of damages in a structure, different types of excitation signals should be employed.

It should be noted that while elastic waves have been widely considered in SHMS, the usage of EM waves has been very limited. In order to show the salient features of EM waves in providing high-resolution image of damages especially in dielectric structures, the application of these waves will be investigated in this study.

The damage identification analysis plays a major role in quantifying the damage in SHMS and can be regarded as the brain of the system. Mathematically speaking, determination of the physical condition of a structure based on sensor measurements is an inverse problem. In its general form, such inverse scattering problem is both nonlinear and typically ill-posed. By ill-posedness, in the sense of Hadamard (Hadamard, 1923), it is meant that one of the following conditions is violated: the existence of the solution; the uniqueness of the solution; or the continuous dependence of the solution on the data (stability condition). The uniqueness condition is generally violated due to the fact that complete data collection from sensors is not practically feasible. In addition, the instability that is most often violated refers to the sensitivity of the solution to noise and measurement error (Haykin, 1999).

When both material properties and geometry of the damage in a structure need to be identified, nonlinear inversion methods such as *Born iterative method* (Chaturvedi and Plumb, 1995), *distorted-Born iterative method* (Weedon et al., 2000), *contrast source method* (Van den Berg and Kleinman, 1997), *genetic algorithm* (Pastorino et al., 2002), and *gradient-based methods* (Rekanos and Raisanen, 2003) are often employed. Although these methods are capable of predicting the damaged material properties in a structure, their application in a SHM system is not practical because of their huge demand of computational time and memory.

To alleviate the deficiencies of the nonlinear inversion methods, linearized inversion methods have been suggested. These methods, mostly based on *Born approximation*, can provide the material properties of the damage as long as the damaged material properties are close to its undamaged material properties and the size of the damage is small compared to the excitation wavelength (Slaney et al., 1984). In some especial cases, e.g. a half-space homogeneous isotropic structure, an *explicit* inversion of the linearized equations can be constructed often with Fourier or related integral transforms (Cui and Chew, 2002). Although this method, so-called *diffraction tomography* (DT), is computationally efficient, it is only applicable for simple structures and needs a uniform and dense measurement collection (Weedon et al., 2000). An alternative to DT is to discretize the linearized integral equations and solve the resulting set of linear algebraic equations numerically, e.g. using a regularized least-squares method (Sabbagh et al., 1988). However, this approach, which needs the analytical or numerical form of Green's functions, is not computationally efficient due to the iteration process involved.

Knowing that identifying damage geometry (or size) with computationally efficient algorithms is the primary and minimum goal of a SHMS, linearized imaging methods should be employed. Linearized imaging methods, which can be considered as an approximation to linearized inversion methods, can only provide the geometries of damages in a structure, sufficient for damage identification. A very important advantage of these methods is that unlike linearized inversion methods, they are well-posed (Zhdanov and Portniaguine, 1997). *Holographic imaging methods*, *synthetic aperture focusing techniques* (*SAFT*), *time-reversal* (*TR*) *techniques*, and *migration algorithms*, mentioned in the literature all belong to this category of linearized imaging methods.

For example, Kim et al. (2004) adopted a holographic technique to identify different damages in concrete slabs. However, only the case of the homogeneous isotropic medium was considered in their formulation. Johansson and Mast (1994) employed a SAFT algorithm in time-domain to construct 3-D images of different flaws and rebars in a concrete slab. Although the method was capable of handling layered medium, the polarization (vector) characteristic of EM waves was not considered and also the quality of the resulting images was not satisfactory. Marklein et al. (2002) also mentioned that SAFT might be extended to EM vector fields and inhomogeneous anisotropic media. Regarding TR techniques, they follow the same principles as migration algorithms. For instance, Kosmas and Rappaport (2005) used the TR technique for breast cancer detection. They considered a 2-D lossy inhomogeneous breast model and used a minimum entropy criterion for finding the optimal time instant when the wave focuses back to the scatterer. Yavuz and Teixeira (2005) also investigated the super-resolution characteristic of the TR technique in focusing back the received signals, resulting from a point source and collected by a linear array, to the original source position in a continuous random lossless media.

Migration algorithms, widely used in seismic prospecting and geophysical exploration, have also been used in EM applications such as ground penetration radar (GPR) and electromagnetic induction (EMI). In GPR applications, displacement currents are dominant due to high frequency of EM field so the field *propagates* into the medium, whereas in EMI applications, conduction currents are dominant due to low frequency of

the EM field, therefore, the field *diffuses* into the medium. Generally, migration algorithms are classified into two groups: poststack and prestack. Prestack migration is computationally more intensive than poststack migration but provides more accurate image, i.e. image with better resolution and higher signal-to-noise ratio. Migration algorithms can also be performed in different domains such as time-space, frequency-space, and frequency-wavenumber (f-k) domains. *Reverse-time migration*, *Kirchhoff migration*, and *phase-shift migration* are some common types of migration algorithms. Although migration algorithms are well established in acoustic and elastic cases and recently in SHM of plates (e.g. Lin and Yuan, 2001; Wang and Yuan, 2005), they are not fully explored in EM case.

The EM migration was originally developed by Zhdanov (1988) and used in geophysical exploration. In this study, Zhdanov (2001) technique for general transient EM field in inhomogeneous isotropic media is adopted and used for damage identification purpose. In addition, to reduce the computational cost of this technique, different imaging conditions are introduced and the resulting images are compared.

This paper is organized in five sections. Section 1 presents some fundamental equations in EM theory used in subsequent sections. EM migration algorithm is formulated in integral equation (IE) form for 3-D case in time-space domain in Section 3. In Section 4, the main steps of the algorithm are described and the methods to reduce the computational cost of this algorithm are also discussed. Section 5 first presents the imaging algorithm specialized for 2-D TM waves. Finally, the effectiveness of the algorithm is demonstrated for 2-D damage detection in a reinforced concrete slab, where a FDTD method has been used to compute all synthetic sensor data, incident field, and migration field.

2. Fundamental equations

This section briefly describes the fundamental equations: Maxwell's equations, their fundamental solutions in terms of dyadic Green's functions, their adjoints, and scattering problem. Some of the details can be found in Felsen and Marcuvitz (1994).

The Maxwell's equations for an inhomogeneous isotropic and lossy medium ($\sigma \neq 0$) including both electric and magnetic current sources are

$$\begin{cases} \nabla \times \boldsymbol{E}(\boldsymbol{r},t) = -\mu_0 \dot{\boldsymbol{H}}(\boldsymbol{r},t) - \boldsymbol{M}(\boldsymbol{r},t) \\ \nabla \times \boldsymbol{H}(\boldsymbol{r},t) = \sigma(\boldsymbol{r})\boldsymbol{E}(\boldsymbol{r},t) + \varepsilon(\boldsymbol{r})\dot{\boldsymbol{E}}(\boldsymbol{r},t) + \boldsymbol{J}(\boldsymbol{r},t) \end{cases} \tag{1}$$

where $\boldsymbol{E}$, $\boldsymbol{H}$, $\boldsymbol{J}$, $\boldsymbol{M}$, μ_0, σ, and ε are electric field intensity (V/m), magnetic field intensity (A/m), prescribed electric current density (A/m^2), prescribed magnetic current density (V/m^2), vacuum permeability (H/m), conductivity (S/m), and permittivity (F/m), respectively. The dot denotes partial derivative with respect to time. Note that the permeability of the medium is assumed to be equal to the vacuum permeability.

Assuming the sources and all fields are zero before some given time $t = t_1$ (zero initial conditions), the electromagnetic fields in an infinite domain can be expressed by four dyadic Green's functions as

$$\begin{aligned} \boldsymbol{E}(\boldsymbol{r},t) &= \int_{V_J}\int_{t_1}^{t} \mathbf{G}^{\mathrm{EJ}}(\boldsymbol{r},t;\boldsymbol{r}',t')\cdot\boldsymbol{J}(\boldsymbol{r}',t')\,\mathrm{d}t'\,\mathrm{d}V' + \int_{V_M}\int_{t_1}^{t} \mathbf{G}^{\mathrm{EM}}(\boldsymbol{r},t;\boldsymbol{r}',t')\cdot\boldsymbol{M}(\boldsymbol{r}',t')\,\mathrm{d}t'\,\mathrm{d}V' \\ \boldsymbol{H}(\boldsymbol{r},t) &= \int_{V_J}\int_{t_1}^{t} \mathbf{G}^{\mathrm{HJ}}(\boldsymbol{r},t;\boldsymbol{r}',t')\cdot\boldsymbol{J}(\boldsymbol{r}',t')\,\mathrm{d}t'\,\mathrm{d}V' + \int_{V_M}\int_{t_1}^{t} \mathbf{G}^{\mathrm{HM}}(\boldsymbol{r},t;\boldsymbol{r}',t')\cdot\boldsymbol{M}(\boldsymbol{r}',t')\,\mathrm{d}t'\,\mathrm{d}V' \end{aligned} \tag{2}$$

where V_J and V_M are the finite volumes occupied by $\boldsymbol{J}$ and $\boldsymbol{M}$, respectively. These dyadic Green's functions satisfy the following equations:

$$\begin{cases} \nabla \times \mathbf{G}^{\mathrm{EJ}} = -\mu_0 \dot{\mathbf{G}}^{\mathrm{HJ}} \\ \nabla \times \mathbf{G}^{\mathrm{HJ}} = \sigma \mathbf{G}^{\mathrm{EJ}} + \varepsilon \dot{\mathbf{G}}^{\mathrm{EJ}} + \delta(\boldsymbol{r}-\boldsymbol{r}')\delta(t-t')\mathbf{I} \end{cases} \tag{3}$$

$$\begin{cases} \nabla \times \mathbf{G}^{\mathrm{EM}} = -\mu_0 \dot{\mathbf{G}}^{\mathrm{HM}} - \delta(\boldsymbol{r}-\boldsymbol{r}')\delta(t-t')\mathbf{I} \\ \nabla \times \mathbf{G}^{\mathrm{HM}} = \sigma \mathbf{G}^{\mathrm{EM}} + \varepsilon \dot{\mathbf{G}}^{\mathrm{EM}} \end{cases} \tag{4}$$

All these dyadic Green's functions satisfy the following initial (causality) conditions:

$$\mathbf{G}(\boldsymbol{r},t;\boldsymbol{r}',t')=0 \quad t\leqslant t' \tag{5}$$

and the associated radiation conditions at infinity.

The physical meaning of each Green dyadic is clear from these equations. For example, $G^{\mathrm{EJ}}_{xz}(\boldsymbol{r},t;\boldsymbol{r}',t')$ denotes the x component of the electric field at point $\boldsymbol{r}$ and time t generated by an impulsive point electric current dipole in the z direction, located at $\boldsymbol{r}=\boldsymbol{r}'$ and excited at $t=t'$.

Adjoint electromagnetic fields play an important role in inverse scattering problem. The equations for adjoint electric and magnetic fields, $\widehat{\boldsymbol{E}}(\boldsymbol{r},t)$ and $\widehat{\boldsymbol{H}}(\boldsymbol{r},t)$, are derived from the original field equation (1) by a temporal and spatial reflection transformation $\partial/\partial t\rightarrow-\partial/\partial t$ and $\nabla\rightarrow-\nabla$, i.e.

$$\begin{cases}-\nabla\times\widehat{\boldsymbol{E}}(\boldsymbol{r},t)=\mu_0\dot{\widehat{\boldsymbol{H}}}(\boldsymbol{r},t)-\widehat{\boldsymbol{M}}(\boldsymbol{r},t)\\ -\nabla\times\widehat{\boldsymbol{H}}(\boldsymbol{r},t)=\sigma(\boldsymbol{r})\widehat{\boldsymbol{E}}(\boldsymbol{r},t)-\varepsilon(\boldsymbol{r})\dot{\widehat{\boldsymbol{E}}}+\widehat{\boldsymbol{J}}(\boldsymbol{r},t)\end{cases} \tag{6}$$

which are subject to reflected initial condition $\widehat{\boldsymbol{E}}=0=\widehat{\boldsymbol{H}}$ for $t\geqslant t_2$ corresponding to excitations $\widehat{\boldsymbol{J}}$ and $\widehat{\boldsymbol{M}}$ that vanish for $t>t_2$ and appropriate reflected radiation conditions. The corresponding adjoint dyadic Green's functions satisfy the following equations:

$$\begin{cases}-\nabla\times\widehat{\mathbf{G}}^{\mathrm{EJ}}=\mu_0\dot{\widehat{\mathbf{G}}}^{\mathrm{HJ}}\\ -\nabla\times\widehat{\mathbf{G}}^{\mathrm{HJ}}=\sigma\widehat{\mathbf{G}}^{\mathrm{EJ}}-\varepsilon\dot{\widehat{\mathbf{G}}}^{\mathrm{EJ}}+\delta(\boldsymbol{r}-\boldsymbol{r}')\delta(t-t')\mathbf{I}\end{cases} \tag{7}$$

$$\begin{cases}-\nabla\times\widehat{\mathbf{G}}^{\mathrm{EM}}=\mu_0\dot{\widehat{\mathbf{G}}}^{\mathrm{HM}}-\delta(\boldsymbol{r}-\boldsymbol{r}')\delta(t-t')\mathbf{I}\\ -\nabla\times\widehat{\mathbf{G}}^{\mathrm{HM}}=\sigma\widehat{\mathbf{G}}^{\mathrm{EM}}-\varepsilon\dot{\widehat{\mathbf{G}}}^{\mathrm{EM}}\end{cases} \tag{8}$$

These adjoint Green's functions are anti-causal, that is,

$$\widehat{\mathbf{G}}(\boldsymbol{r},t;\boldsymbol{r}',t')=0 \quad t\geqslant t' \tag{9}$$

and satisfy associated reflected radiation conditions.

Linearity of the adjoint equations (6) indicates that the adjoint fields are representable in a form similar to those in Eq. (2):

$$\begin{aligned}\widehat{\boldsymbol{E}}(\boldsymbol{r},t)&=\int_{V_{\hat{J}}}\int_{t_2}^{t}\widehat{\mathbf{G}}^{\mathrm{EJ}}(\boldsymbol{r},t;\boldsymbol{r}',t')\cdot\widehat{\boldsymbol{J}}(\boldsymbol{r}',t')\,\mathrm{d}t'\,\mathrm{d}V'+\int_{V_{\hat{M}}}\int_{t_2}^{t}\widehat{\mathbf{G}}^{\mathrm{EM}}(\boldsymbol{r},t;\boldsymbol{r}',t')\cdot\widehat{\boldsymbol{M}}(\boldsymbol{r}',t')\,\mathrm{d}t'\,\mathrm{d}V'\\ \widehat{\boldsymbol{H}}(\boldsymbol{r},t)&=\int_{V_{\hat{J}}}\int_{t_2}^{t}\widehat{\mathbf{G}}^{\mathrm{HJ}}(\boldsymbol{r},t;\boldsymbol{r}',t')\cdot\widehat{\boldsymbol{J}}(\boldsymbol{r}',t')\,\mathrm{d}t'\,\mathrm{d}V'+\int_{V_{\hat{M}}}\int_{t_2}^{t}\widehat{\mathbf{G}}^{\mathrm{HM}}(\boldsymbol{r},t;\boldsymbol{r}',t')\cdot\widehat{\boldsymbol{M}}(\boldsymbol{r}',t')\,\mathrm{d}t'\,\mathrm{d}V'\end{aligned} \tag{10}$$

where finite $V_{\hat{J}}$ and $V_{\hat{M}}$ are the volumes occupied by $\widehat{\boldsymbol{J}}$ and $\widehat{\boldsymbol{M}}$, respectively. Note that in the above relations: $t\leqslant t'\leqslant t_2$. In addition, adjoint dyadic Green's functions have the following relationships with dyadic Green's functions:

$$\begin{cases}\widehat{\mathbf{G}}^{\mathrm{EJ}}(\boldsymbol{r},t;\boldsymbol{r}',t')=\mathbf{G}^{\mathrm{EJ}^{\mathrm{T}}}(\boldsymbol{r}',t';\boldsymbol{r},t)\\ \widehat{\mathbf{G}}^{\mathrm{EM}}(\boldsymbol{r},t;\boldsymbol{r}',t')=\mathbf{G}^{\mathrm{HJ}^{\mathrm{T}}}(\boldsymbol{r}',t';\boldsymbol{r},t)\end{cases}\quad\begin{cases}\widehat{\mathbf{G}}^{\mathrm{HJ}}(\boldsymbol{r},t;\boldsymbol{r}',t')=\mathbf{G}^{\mathrm{EM}^{\mathrm{T}}}(\boldsymbol{r}',t';\boldsymbol{r},t)\\ \widehat{\mathbf{G}}^{\mathrm{HM}}(\boldsymbol{r},t;\boldsymbol{r}',t')=\mathbf{G}^{\mathrm{HM}^{\mathrm{T}}}(\boldsymbol{r}',t';\boldsymbol{r},t)\end{cases} \tag{11}$$

where superscript T indicates transpose operator.

Now, let us consider the scattering problem of a finite scatterer (damage) occupying the volume V_{scat}, embedded in a background medium (host structure), and excited by electric and/or magnetic current sources at $t_1=0$. Eq. (1) holds in the two domains with

$$\sigma,\varepsilon=\begin{cases}\sigma(\boldsymbol{r}),\varepsilon(\boldsymbol{r}) & \boldsymbol{r}\subset V_{\mathrm{scat}}\\ \sigma_{\mathrm{b}}(\boldsymbol{r}),\varepsilon_{\mathrm{b}}(\boldsymbol{r}) & \boldsymbol{r}\not\subset V_{\mathrm{scat}}\end{cases} \tag{12}$$

where subscript 'b' implies background. The total field can be decomposed into incident and scattered fields, i.e.,

$$\begin{aligned} \boldsymbol{E} &= \boldsymbol{E}_{\text{inc}} + \boldsymbol{E}_{\text{scat}} \\ \boldsymbol{H} &= \boldsymbol{H}_{\text{inc}} + \boldsymbol{H}_{\text{scat}} \end{aligned} \tag{13}$$

The incident field is defined as the field due to the sources, $\boldsymbol{J}$ and $\boldsymbol{M}$, in the absence of the damage; therefore, it satisfies Eq. (1) in the background medium,

$$\begin{cases} \nabla \times \boldsymbol{E}_{\text{inc}} = -\mu_0 \dot{\boldsymbol{H}}_{\text{inc}} - \boldsymbol{M} \\ \nabla \times \boldsymbol{H}_{\text{inc}} = \sigma_{\text{b}} \boldsymbol{E}_{\text{inc}} + \varepsilon_{\text{b}} \dot{\boldsymbol{E}}_{\text{inc}} + \boldsymbol{J} \end{cases} \tag{14}$$

Equations for the scattered field can be derived using Eq. (1), (13) and (14) as

$$\begin{cases} \nabla \times \boldsymbol{E}_{\text{scat}} = -\mu_0 \dot{\boldsymbol{H}}_{\text{scat}} \\ \nabla \times \boldsymbol{H}_{\text{scat}} = \sigma_{\text{b}} \boldsymbol{E}_{\text{scat}} + \varepsilon_{\text{b}} \dot{\boldsymbol{E}}_{\text{scat}} + [\Delta\sigma \boldsymbol{E} + \Delta\varepsilon \dot{\boldsymbol{E}}] \end{cases} \tag{15}$$

where *contrast medium parameters* are defined as

$$\begin{aligned} \Delta\varepsilon &= \varepsilon - \varepsilon_{\text{b}} \\ \Delta\sigma &= \sigma - \sigma_{\text{b}} \end{aligned} \tag{16}$$

In view of Eq. (1) and (2), the scattered field in Eq. (15) can be expressed in terms of background dyadic Green's functions as

$$\begin{aligned} \boldsymbol{E}_{scat}(\boldsymbol{r}, t) &= \int_0^t \int_{V_{scat}} \mathbf{G}_b^{EJ}(\boldsymbol{r}, t; \boldsymbol{r}', t') \cdot \left[\Delta\sigma(\boldsymbol{r}') \boldsymbol{E}(\boldsymbol{r}', t') + \Delta\varepsilon(\boldsymbol{r}') \dot{\boldsymbol{E}}(\boldsymbol{r}', t')\right] \mathrm{d}V' \, \mathrm{d}t' \\ \boldsymbol{H}_{scat}(\boldsymbol{r}, t) &= \int_0^t \int_{V_{scat}} \mathbf{G}_b^{HJ}(\boldsymbol{r}, t; \boldsymbol{r}', t') \cdot \left[\Delta\sigma(\boldsymbol{r}') \boldsymbol{E}(\boldsymbol{r}', t') + \Delta\varepsilon(\boldsymbol{r}') \dot{\boldsymbol{E}}(\boldsymbol{r}', t')\right] \mathrm{d}V' \, \mathrm{d}t' \end{aligned} \tag{17}$$

In inverse scattering problems, one attempts to quantify the material properties of the scatterer (damage) from the scattered field measured outside the scatterer. This inverse problem is nonlinear in contrast medium parameters because the measured scattered field depends on the total field, which in turn is also a function of the contrast parameters.

3. The electromagnetic migration

The basic principles of electromagnetic migration were first formulated by Zhdanov (1988) for the case of diffusive EM field in geophysical exploration. He introduced time-domain EM migration as the solution of the boundary value problem in the semi-infinite space (the earth) for the adjoint Maxwell's equations, in which the boundary values of the migration field on the observation surface are determined by the measured EM field. Zhdanov and Portniaguine (1997) showed that EM migration can be associated with the inverse problem solution: First, they introduced the EM energy flow of the *residual field*, the difference between the simulated (calculated) EM field for some given model and the measured EM field, through the observation surface as a functional of the conductivity distribution in the model. Then, it was shown the EM migration can be considered as the first iteration in the general EM inversion procedure, based on the minimization of the residual field energy flow through the observation surface. They called their iterative method, the *iterative EM migration*. The extension of this algorithm for the case of general transient EM field, where both conductivity and permittivity images are obtained, was made by Zhdanov (2001).

In this study, the EM migration algorithm for the general transient EM field in inhomogeneous isotropic media is adopted and used for damage identification purpose. In addition, to reduce the computational cost of the original algorithm, different imaging conditions including zero-time imaging condition (poststack scheme) are introduced and the resulting images are compared.

Consider a transient electromagnetic experiment in which an electromagnetic source (actuator) at position $\boldsymbol{s}_j$ is excited with a source waveform $f(t)$, and the transient electric and magnetic field, $\boldsymbol{E}^d(\boldsymbol{r}, t)$ and $\boldsymbol{H}^d(\boldsymbol{r}, t)$, are measured over an observation surface S from time $t = 0$ to $t = T$. It is assumed that the source and all fields

are zero before $t = 0$. The total instantaneous power flow of the residual field through the observation surface is

$$p(t) = \int_S (\Delta \boldsymbol{E} \times \Delta \boldsymbol{H}) \cdot \boldsymbol{n} \, \mathrm{d}S \tag{18}$$

where $\boldsymbol{n}$ is a unit normal vector pointing outward of S (pointing away the scattering region) and the data residuals are given by

$$\begin{aligned} \Delta \boldsymbol{E}(\boldsymbol{r}, t) &= \boldsymbol{E}^d(\boldsymbol{r}, t) - \boldsymbol{E}(\boldsymbol{r}, t) \\ \Delta \boldsymbol{H}(\boldsymbol{r}, t) &= \boldsymbol{H}^d(\boldsymbol{r}, t) - \boldsymbol{H}(\boldsymbol{r}, t) \end{aligned} \tag{19}$$

where $\boldsymbol{E}^d(\boldsymbol{r}, t)$ and $\boldsymbol{H}^d(\boldsymbol{r}, t)$ are the measured EM field, and $\boldsymbol{E}(\boldsymbol{r}, t)$ and $\boldsymbol{H}(\boldsymbol{r}, t)$ are the simulated (calculated) EM field for a given model.

It has been shown (Zhdanov, 2002) that the power flow of the residual field is non-negative, i.e. $p(t) \geqslant 0$. Note that there are no external EM sources inside the region surrounded by the observation surface S (the scattering region). Based on the non-negativeness property of the power flow, the following functional is introduced:

$$P(\sigma, \varepsilon) = \int_0^T \int_S (\Delta \boldsymbol{E} \times \Delta \boldsymbol{H}) \cdot \boldsymbol{n} \, \mathrm{d}S \, \mathrm{d}t \tag{20}$$

Thus, the EM inversion problem can be recast as the minimization of this residual-field energy-flow functional. The dependence of the functional P on the *model parameters* (i.e. σ and ε) comes from the implicit dependence of the calculated fields $\boldsymbol{E}(\boldsymbol{r}, t)$ and $\boldsymbol{H}(\boldsymbol{r}, t)$ on σ and ε.

A gradient type method is usually applied for the solution of the minimum energy flow problem, which is based on computing the gradient direction for P and decreasing this functional iteratively in the space of the inverse problem solutions. Let $\sigma^{(n)}$ and $\varepsilon^{(n)}$ be the conductivity and permittivity of the model at the nth iteration and let $\gamma_\sigma^{(n)}$ and $\gamma_\varepsilon^{(n)}$ be the gradients of P with respect to $\sigma^{(n)}$ and $\varepsilon^{(n)}$. In a gradient or steepest descent algorithm, the model is updated by steps along the gradient directions (Wang et al., 1994):

$$\begin{aligned} \sigma^{(n+1)} &= \sigma^{(n)} - \alpha^{(n)} \gamma_\sigma^{(n)} \\ \varepsilon^{(n+1)} &= \varepsilon^{(n)} - \beta^{(n)} \gamma_\varepsilon^{(n)} \end{aligned} \tag{21}$$

where α and β are positive step lengths and their optimal values at each iteration are usually obtained using a line-search method. For continuous models, the gradients are actually *Frechet derivatives* of P, i.e.

$$\gamma_\sigma = \frac{\partial P}{\partial \sigma} \tag{22}$$

$$\gamma_\varepsilon = \frac{\partial P}{\partial \varepsilon} \tag{23}$$

These are linear functionals such that for small perturbations $\delta\sigma$ and $\delta\varepsilon$ about the current model,

$$\begin{aligned} \delta P &= P(\sigma + \delta\sigma, \varepsilon + \delta\varepsilon) - P(\sigma, \varepsilon) \\ &= \langle \gamma_\sigma, \delta\sigma \rangle_{H_M} + \langle \gamma_\varepsilon, \delta\varepsilon \rangle_{H_M} + \text{terms of the order } \left\{ \|\delta\sigma\|_{H_M}^2, \|\delta\varepsilon\|_{H_M}^2 \right\} \end{aligned} \tag{24}$$

where $\langle \cdot, \cdot \rangle_{H_M}$ and $\| \cdot \|_{H_M}$ indicate dot product and norm on the Hilbert space of models, respectively, with the following definitions:

$$\langle \delta m_1, \delta m_2 \rangle_{H_M} = \int_{V'} \delta m_1(\boldsymbol{r}') \delta m_2(\boldsymbol{r}') \, \mathrm{d}V' \quad \forall \delta m_1, \delta m_2 \in H_M \tag{25}$$

$$\|\delta m\|_{H_M}^2 = \langle \delta m, \delta m \rangle_{H_M} \tag{26}$$

where V' is the domain over which the model is allowed to vary and δm stands for either $\delta\sigma$ or $\delta\varepsilon$.

It should be noted that the most important step in an iterative gradient method is to calculate the gradients of the functional with respect to the model parameters at each iteration. In view of relation (24) and definitions (25) and (26), the first variation of P is:

$$\delta^{(1)}P = \langle \gamma_\sigma, \delta\sigma \rangle_{H_M} + \langle \gamma_\varepsilon, \delta\varepsilon \rangle_{H_M} = \int_{V'} \gamma_\sigma(\boldsymbol{r}')\delta\sigma(\boldsymbol{r}')\,\mathrm{d}V' + \int_{V'} \gamma_\varepsilon(\boldsymbol{r}')\delta\varepsilon(\boldsymbol{r}')\,\mathrm{d}V' \tag{27}$$

The first variation of P using Eq. (20) together with Eq. (19) can also be obtained as

$$\delta^{(1)}P = -\int_0^T \int_S (\Delta\boldsymbol{E} \times \delta\boldsymbol{H} - \Delta\boldsymbol{H} \times \delta\boldsymbol{E}) \cdot \boldsymbol{n}\,\mathrm{d}S\,\mathrm{d}t \tag{28}$$

where $\delta\boldsymbol{E}(\boldsymbol{r},t)$ and $\delta\boldsymbol{H}(\boldsymbol{r},t)$ are the change in the calculated data when the conductivity and permittivity of the model are changed. The first variation of the Maxwell's equations (1) with respect to model parameters is

$$\begin{cases} \nabla \times \delta\boldsymbol{E} = -\mu_0 \delta\dot{\boldsymbol{H}} \\ \nabla \times \delta\boldsymbol{H} = \sigma\delta\boldsymbol{E} + \varepsilon\delta\dot{\boldsymbol{E}} + \left[\delta\sigma\boldsymbol{E} + \delta\varepsilon\dot{\boldsymbol{E}}\right] \end{cases} \tag{29}$$

The term in the bracket can be considered as an effective electric current source for the perturbed fields. Using Eq. (2), these perturbed fields can be written in terms of dyadic Green's functions as

$$\delta\boldsymbol{E}(\boldsymbol{r},t) = \int_0^t \int_{V'} \mathbf{G}^{\mathrm{EJ}}(\boldsymbol{r},t;\boldsymbol{r}',t') \cdot \left[\delta\sigma(\boldsymbol{r}')\boldsymbol{E}(\boldsymbol{r}',t') + \delta\varepsilon(\boldsymbol{r}')\dot{\boldsymbol{E}}(\boldsymbol{r}',t')\right] \mathrm{d}V'\,\mathrm{d}t' \tag{30}$$

$$\delta\boldsymbol{H}(\boldsymbol{r},t) = \int_0^t \int_{V'} \mathbf{G}^{\mathrm{HJ}}(\boldsymbol{r},t;\boldsymbol{r}',t') \cdot \left[\delta\sigma(\boldsymbol{r}')\boldsymbol{E}(\boldsymbol{r}',t') + \delta\varepsilon(\boldsymbol{r}')\dot{\boldsymbol{E}}(\boldsymbol{r}',t')\right] \mathrm{d}V'\,\mathrm{d}t' \tag{31}$$

Substituting Eq. (30) and (31) into (28), using relation (27), interchanging the time integrals, and then using relations (11), the gradients of P are obtained as

$$\gamma_\sigma(\boldsymbol{r}') = \frac{\partial P}{\partial \sigma} = \int_0^T \boldsymbol{E}^m_\Delta(\boldsymbol{r}',t') \cdot \boldsymbol{E}(\boldsymbol{r}',t')\,\mathrm{d}t' \tag{32}$$

$$\gamma_\varepsilon(\boldsymbol{r}') = \frac{\partial P}{\partial \varepsilon} = \int_0^T \boldsymbol{E}^m_\Delta(\boldsymbol{r}',t') \cdot \dot{\boldsymbol{E}}(\boldsymbol{r}',t')\,\mathrm{d}t' \tag{33}$$

where

$$\boldsymbol{E}^m_\Delta(\boldsymbol{r}',t') = \int_S \int_T^{t'} \left\{ \widehat{\mathbf{G}}^{\mathrm{EM}}(\boldsymbol{r}',t';\boldsymbol{r},t) \cdot [\boldsymbol{n} \times \Delta\boldsymbol{E}(\boldsymbol{r},t)] - \widehat{\mathbf{G}}^{\mathrm{EJ}}(\boldsymbol{r}',t';\boldsymbol{r},t) \cdot [\boldsymbol{n} \times \Delta\boldsymbol{H}(\boldsymbol{r},t)] \right\} \mathrm{d}t\,\mathrm{d}S \tag{34}$$

For the first iteration of the inverse problem, the most logical initial guess of the model parameters are the background (host structure) parameters. Thus, the following changes will be applied

$$\begin{cases} \sigma \to \sigma_{\mathrm{b}} \\ \varepsilon \to \varepsilon_{\mathrm{b}} \end{cases} \Rightarrow \begin{cases} \boldsymbol{E} \to \boldsymbol{E}_{\mathrm{inc}} \\ \boldsymbol{H} \to \boldsymbol{H}_{\mathrm{inc}} \end{cases}, \quad \begin{cases} \Delta\boldsymbol{E} \to \boldsymbol{E}^d - \boldsymbol{E}_{\mathrm{inc}} = \boldsymbol{E}^d_{\mathrm{scat}} \\ \Delta\boldsymbol{H} \to \boldsymbol{H}^d - \boldsymbol{H}_{\mathrm{inc}} = \boldsymbol{H}^d_{\mathrm{scat}} \end{cases}, \quad \begin{cases} \widehat{\mathbf{G}}^{\mathrm{EJ}} \to \widehat{\mathbf{G}}^{\mathrm{EJ}}_{\mathrm{b}} \\ \widehat{\mathbf{G}}^{\mathrm{EM}} \to \widehat{\mathbf{G}}^{\mathrm{EM}}_{\mathrm{b}} \end{cases} \tag{35}$$

Then, Eq. (34) for the migration residual electric field is changed into the following equation for the *migration scattered electric field*:

$$\boldsymbol{E}^m_{\mathrm{scat}}(\boldsymbol{r}',t') = \int_S \int_T^{t'} \left\{ \widehat{\mathbf{G}}^{\mathrm{EJ}}_{\mathrm{b}}(\boldsymbol{r}',t';\boldsymbol{r},t) \cdot \left[-\boldsymbol{n} \times \boldsymbol{H}^d_{\mathrm{scat}}(\boldsymbol{r},t)\right] + \widehat{\mathbf{G}}^{\mathrm{EM}}_{\mathrm{b}}(\boldsymbol{r}',t';\boldsymbol{r},t) \cdot \left[\boldsymbol{n} \times \boldsymbol{E}^d_{\mathrm{scat}}(\boldsymbol{r},t)\right] \right\} \mathrm{d}t\,\mathrm{d}S \tag{36}$$

In this case, the negative gradients of P with respect to the model parameters in Eq. (32) and (33) are defined as *apparent contrast parameters*, i.e.

$$\Delta\widehat{\sigma}(\boldsymbol{r}') = -\int_0^T \boldsymbol{E}^m_{\mathrm{scat}}(\boldsymbol{r}',t') \cdot \boldsymbol{E}_{\mathrm{inc}}(\boldsymbol{r}',t')\,\mathrm{d}t' \tag{37}$$

$$\Delta\widehat{\varepsilon}(\boldsymbol{r}') = -\int_0^T \boldsymbol{E}^m_{\mathrm{scat}}(\boldsymbol{r}',t') \cdot \dot{\boldsymbol{E}}_{\mathrm{inc}}(\boldsymbol{r}',t')\,\mathrm{d}t' \tag{38}$$

The images constructed from Eq. (37) and (38) are called the *conductivity* and *permittivity images*, respectively.

In view of Eq. (10), it can be observed that the integral equation (36) with $T \geqslant t \geqslant t'$ has the appropriate form for propagation with the adjoint Green's functions $\widehat{\mathbf{G}}_{\mathrm{b}}^{\mathrm{EM}}$ and $\widehat{\mathbf{G}}_{\mathrm{b}}^{\mathrm{EJ}}$. In fact, $\widehat{\mathbf{G}}_{\mathrm{b}}^{\mathrm{EM}}(\boldsymbol{r}', t'; \boldsymbol{r}, t)(\widehat{\mathbf{G}}_{\mathrm{b}}^{\mathrm{EJ}}(\boldsymbol{r}', t'; \boldsymbol{r}, t))$ gives the electric field at $\boldsymbol{r}'$ and time t' caused by a magnetic (electric) current source, here $\boldsymbol{n} \times \boldsymbol{E}^d_{\mathrm{scat}}(\boldsymbol{r}, t)(-\boldsymbol{n} \times \boldsymbol{H}^d_{\mathrm{scat}}(\boldsymbol{r}, t))$, radiating at $\boldsymbol{r}$ at a later time t. Note that ordinary scattered fields, governed by the Maxwell's equations, propagate from damage to the observation surface, whereas migration scattered fields, governed by the adjoint Maxwell's equations, propagate from observation surface to their original place, the damage. Mathematically, the imaging formulas (37) or (38) represent negative zero-lag cross-correlation of the migration scattered electric field with incident electric field or time derivative of incident electric field, respectively.

In practice, the measurement is performed at discrete locations $\boldsymbol{r}_i \in \{\boldsymbol{r}_1, \ldots, \boldsymbol{r}_N\}$ on a planar observation surface. Then, the relation (36) can be written as

$$\boldsymbol{E}^m_{\mathrm{scat}}(\boldsymbol{r}', t') = \sum_i \int_T^{t'} \left\{ \widehat{\mathbf{G}}_{\mathrm{b}}^{\mathrm{EJ}}(\boldsymbol{r}', t'; \boldsymbol{r}_i, t) \cdot \left[-\boldsymbol{n} \times \boldsymbol{H}^d_{\mathrm{scat}}(\boldsymbol{r}_i, t) \right] + \widehat{\mathbf{G}}_{\mathrm{b}}^{\mathrm{EM}}(\boldsymbol{r}', t'; \boldsymbol{r}_i, t) \cdot \left[\boldsymbol{n} \times \boldsymbol{E}^d_{\mathrm{scat}}(\boldsymbol{r}_i, t) \right] \right\} \mathrm{d}t \tag{39}$$

Considering Eq. (10) and the adjoint field equations (6), it can be inferred that the migration scattered electric field $\boldsymbol{E}^m_{\mathrm{scat}}(\boldsymbol{r}', t')$ satisfies equations adjoint to Maxwell's equations and that the source terms for these adjoint equations are $\boldsymbol{n} \times \boldsymbol{E}^d_{\mathrm{scat}}(\boldsymbol{r}_i, t)$ and $-\boldsymbol{n} \times \boldsymbol{H}^d_{\mathrm{scat}}(\boldsymbol{r}_i, t)$ at all the sensor locations radiating as magnetic and electric current sources in reverse time, respectively; i.e.,

$$\begin{cases} -\nabla \times \boldsymbol{E}^m_{\mathrm{scat}}(\boldsymbol{r}, t) = \mu_0 \dot{\boldsymbol{H}}^m_{\mathrm{scat}}(\boldsymbol{r}, t) - \sum_i \left[\boldsymbol{n} \times \boldsymbol{E}^d_{\mathrm{scat}}(\boldsymbol{r}_i, t) \right] \delta(\boldsymbol{r} - \boldsymbol{r}_i) \\ -\nabla \times \boldsymbol{H}^m_{\mathrm{scat}}(\boldsymbol{r}, t) = \sigma_{\mathrm{b}} \boldsymbol{E}^m_{\mathrm{scat}}(\boldsymbol{r}, t) - \varepsilon_{\mathrm{b}} \dot{\boldsymbol{E}}^m_{\mathrm{scat}}(\boldsymbol{r}, t) + \sum_i \left[-\boldsymbol{n} \times \boldsymbol{H}^d_{\mathrm{scat}}(\boldsymbol{r}_i, t) \right] \delta(\boldsymbol{r} - \boldsymbol{r}_i) \end{cases} \tag{40}$$

where $t = T \cdots 0$.

Unlike Eq. (40) in which the measurement data are treated as sources, Zhdanov defined the migration scattered field as the solution of the boundary value problem for the homogeneous adjoint Maxwell's equations, in which the time-dependent boundary values of the migration field on the observation surface are determined by the measured scattered fields; i.e.

$$\begin{cases} -\nabla \times \boldsymbol{E}^m_{\mathrm{scat}}(\boldsymbol{r}, t) = \mu_0 \dot{\boldsymbol{H}}^m_{\mathrm{scat}}(\boldsymbol{r}, t) \\ -\nabla \times \boldsymbol{H}^m_{\mathrm{scat}}(\boldsymbol{r}, t) = \sigma_{\mathrm{b}} \boldsymbol{E}^m_{\mathrm{scat}}(\boldsymbol{r}, t) - \varepsilon_{\mathrm{b}} \dot{\boldsymbol{E}}^m_{\mathrm{scat}}(\boldsymbol{r}, t) \end{cases} \tag{41a}$$

$$\text{BC's}: \begin{cases} \boldsymbol{n} \times \boldsymbol{E}^m_{\mathrm{scat}}(\boldsymbol{r}_i, t) = \boldsymbol{n} \times \boldsymbol{E}^d_{\mathrm{scat}}(\boldsymbol{r}_i, t) \\ \boldsymbol{n} \times \boldsymbol{H}^m_{\mathrm{scat}}(\boldsymbol{r}_i, t) = \boldsymbol{n} \times \boldsymbol{H}^d_{\mathrm{scat}}(\boldsymbol{r}_i, t) \end{cases} \quad \boldsymbol{r}_i \in \{\boldsymbol{r}_1, \ldots, \boldsymbol{r}_N\}; \quad t = T \cdots 0 \tag{41b}$$

It should be noted that the migration algorithms will not provide a complete image of damage geometry if only one actuator is used. The reason is that each actuator can illuminate only partial geometry of the damage. In case of multiple actuator excitations with actuator positions at $\boldsymbol{s}_j \in \{\boldsymbol{s}_1, \ldots, \boldsymbol{s}_M\}$, the imaging formulas (37) and (38) become

$$\Delta \widehat{\sigma}(\boldsymbol{r}') = -\sum_j \int_0^T \boldsymbol{E}^m_{\mathrm{scat}}(\boldsymbol{r}', t' \mid \boldsymbol{s}_j) \cdot \boldsymbol{E}_{\mathrm{inc}}(\boldsymbol{r}', t' \mid \boldsymbol{s}_j) \, \mathrm{d}t' \tag{42}$$

$$\Delta \widehat{\varepsilon}(\boldsymbol{r}') = -\sum_j \int_0^T \boldsymbol{E}^m_{\mathrm{scat}}(\boldsymbol{r}', t' \mid \boldsymbol{s}_j) \cdot \dot{\boldsymbol{E}}_{\mathrm{inc}}(\boldsymbol{r}', t' \mid \boldsymbol{s}_j) \, \mathrm{d}t' \tag{43}$$

4. Imaging steps in electromagnetic migration

The EM migration algorithm consists of the following three steps; similar to *prestack migration* (Claerbout, 1971):

(1) Computation of the migration (back propagation) of the measured scattered field generated by the *j*th actuator, i.e. integral equations (39) or differential equations (40) or (41). In migration literature, the measured scattered field collected by the sensors on the observation surface due to a common actuator is called *common-shot gather* (*experiment*).
(2) Application of zero-lag cross-correlation of the migration scattered field with the incident field or its time derivative caused by the *j*th actuator, i.e. integral equations (42) and (43), which provides a partial image of damage geometry from the *j*th actuator. This step is generally called *zero-lag cross-correlation imaging condition* in migration literature (Claerbout, 1971).
(3) Summation of partial images obtained by different actuator excitations. In other words, each common-source gather is migrated independently to produce a partial image; the final composite image is obtained by stacking over the partial images (Chang and McMechan, 1994). In fact, this stacking process after the migration enhances the signal-to-noise ratio (Lin and Yuan, in press).

To lower computational cost of the zero-lag cross-correlation imaging condition in prestack migration, in step (2), Chang and McMechan (1986) developed *excitation-time imaging condition*. First, the *excitation time* (defined as the moment when a point in image area, called image point, is excited by the wave energy from the actuator) from an actuator to each image point is computed and kept in an *excitation-time* (*one-way travel time*) *table*. Then, instead of applying zero-lag cross-correlation imaging condition which needs the computation of incident field or its time derivative at each image point at all times, the image at a specified point is considered as the amplitude of the computed migration scattered field at that point at its excitation time. Although the excitation-time imaging condition is not as accurate as the zero-lag cross-correlation one, it reduces the computational cost dramatically.

Several methods have been used to calculate the excitation-time table in acoustic and elastic wave cases such as ray tracing (Chang and McMechan, 1986), finite difference (FD) solution of eikonal equation (Vidale, 1988 and Zhu and Lines, 1997), and FD solution of wave equation (Chang and McMechan, 1994 and Loewenthal and Hu, 1991). It should be noted that the results obtained by the third method is more accurate because it is based on the wave equation while the first two methods rely on the high-frequency ray approximation. Although the third method demands the highest computational cost, it remains the best choice for accurate damage identification. The reason is that the computation of the excitation-time table is performed before the monitoring stage.

Loewenthal and Hu (1991) suggested two criteria for calculating the excitation-time table using the FD solution of the acoustic wave equation:

(a) Maximum amplitude criterion (maximum-energy arrival criterion): The travel time of an image point is calculated at the moment the incident wave has maximum amplitude at the image point.
(b) Minimum time criterion (first-arrival criterion): The travel time of an image point is calculated at the moment the incident wave hits the image point.

Audebert et al. (1997) showed that Kirchhoff migration using *maximum-energy travel time* significantly improve the images quality especially in areas of complex structures compared to the *first-arrival travel time*.

In order to enhance the resolution of the images obtained by the excitation-time imaging condition with (a) and (b) criteria, a modified excitation-time imaging condition is introduced. In this modified condition, the following approximation for any component of the incident electric field (or its time derivative) is considered:

$$e_{\mathrm{inc}}(\boldsymbol{r}', t' \mid \boldsymbol{s}_j) \cong A_e(\boldsymbol{r}' \mid \boldsymbol{s}_j)\delta\big(t' - \tau_e(\boldsymbol{r}' \mid \boldsymbol{s}_j)\big) \tag{44}$$

where $\boldsymbol{r}'$, $\boldsymbol{s}_j$, $\tau_e(\boldsymbol{r}'|\boldsymbol{s}_j)$, and $A_e(\boldsymbol{r}'|\boldsymbol{s}_j)$ are an arbitrary image point position, the *j*th actuator location, the travel time of the e_{inc} component from the actuator to the image point, and the amplitude of the e_{inc} field component at $t' = \tau_e$, respectively. Note that in the excitation-time imaging condition only the travel time of the incident field or its time derivative is used, whereas in the modified condition both travel time and amplitude of the field are taken into account.

In this paper, the application of the zero-lag cross-correlation, the excitation-time, and the modified excitation-time imaging conditions (based on the first-arrival or maximum-energy travel time) are examined.

Another way to reduce computational cost of the EM migration is to perform it in a poststack scheme. In *poststack migration*, the recorded data should be collected in a monostatic setup (zero-offset experiment), i.e. the actuators and the sensors are collocated.

The concept of poststack migrations is based on the *exploding reflector model* (Scales, 1997): The data recorded in the zero-offset experiment is the same that would be recorded if we placed actuators along the damage boundary and fired them off with a strength proportional to the reflection coefficient at $t = 0$ in the medium having one half of the original velocity. This means that if we somehow run the zero-offset wave field recorded at the surface backward in time, then by evaluating the results at $t = 0$ (*zero-time imaging condition*), we would have a picture of the reflection event as it occurred, provided we use half the original velocity when we run the recorded field backward in time. Therefore, the image can be simply obtained by applying the zero-time imaging condition to the migration scattered field computed in a half original velocity host structure (or a 2:1 scaled host structure).

Unfortunately, the exploding reflector model concept is not quantitatively correct (some of the shortcomings are described in Claerbout and Black (2001) and Chen and Huang (1998)). Also, the signal-to-noise ratio (SNR) of prestack migration is higher than that of poststack migration (Gray, 1999). Moreover, Chen and Schuster (1999) showed in acoustic case that prestack images have better dynamic range (DNR) than that of the poststack images. In spite of these shortcomings, poststack migration concept is also applied in this study due to its computational efficiency.

A simple way to compute the migration scattered field is to use FD discretization of the differential equations (40) or (41). In migration literature, when migration scattered field computation is carried out by FD discretization of the full wave equation in time-space domain, the method is generally called *reverse-time migration* (*RTM*). Ability to consider any inhomogeneities in the host structure, high accuracy and simple programming are some advantages of RTM. Zhu and Lines (1997) showed, in acoustic case, that reverse-time wave equation extrapolation procedure had also the capability of implicitly interpolating missing recorded traces (data) in FD grid, as long as net data sampling is not aliased locally either temporally or spatially. This healing characteristic is very important in a SHMS because not only will the system be able to operate with fewer numbers of sensors but it will be more robust when some of the sensors lose their functions. However, including any discontinuity in the material property model of the host structure will generate internal reflections during migration of the recorded scattered field and forward propagation of incident field (or its time derivative) and thus causes artifacts in the image (Biondi, 2004). These artifacts are generated due to the use of full two-way wave equation.

In this paper, all synthetic sensor data, incident wavefield, and migration wavefield are computed with a FDTD method.

5. Numerical results

This section first presents the imaging algorithm specialized for 2-D transverse magnetic wave. Then, the effectiveness of the EM migration algorithm is demonstrated for 2-D damage detection in a reinforced concrete slab.

A two-dimensional EM field can be generated when neither EM field excitation nor model geometry has any variation in one specified direction, say y-direction. Then, all partial derivatives of the fields with respect to y are equal to zero and the EM field can be separated into two decoupled transverse electric (TE) and transverse magnetic (TM) fields. In TM field, the magnetic vector is transverse to the y-direction and perpendicular to the electric vector (i.e. E_y, H_x, and H_z). The TM field can be excited by an electric current density $J_y(x, z, t)$. Let us consider the z-axis downward from the upper surface toward the host structure and the measurement line parallel to the x-axis ($z > 0$). Therefore, $\boldsymbol{n} = -\boldsymbol{k}$, where $\boldsymbol{k}$ is the z-axis unit vector. Then, EM migration imaging formulas (42) and (43) reduce to:

$$\Delta\widehat{\sigma}(x', z') = -\sum_j \int_0^T E^m_{y;\mathrm{scat}}(x', z', t') E_{y;\mathrm{inc}}(x', z', t')\,\mathrm{d}t' \tag{45}$$

$$\Delta\widehat{\varepsilon}(x', z') = -\sum_j \int_0^T E^m_{y;\mathrm{scat}}(x', z', t') \dot{E}_{y;\mathrm{inc}}(x', z', t')\,\mathrm{d}t' \tag{46}$$

where the case of multiple actuator excitations at positions (x_j, z_j) is considered through the j summation. However, the dependency of the field on the actuator position is not shown for the sake of brevity.

The migration scattered electric field in the above equations can be computed from the following adjoint Maxwell's equations while the measurement scattered fields are treated *as sources*:

$$\begin{cases} \dfrac{\partial E^m_{y;\mathrm{scat}}}{\partial z} = \mu_0 \dfrac{\partial H^m_{x;\mathrm{scat}}}{\partial t} - \displaystyle\sum_i E^d_{y;\mathrm{scat}}(x_i, z_i, t)\delta(x - x_i)\delta(z - z_i) \\ -\dfrac{\partial H^m_{x;\mathrm{scat}}}{\partial z} + \dfrac{\partial H^m_{z;\mathrm{scat}}}{\partial x} = \sigma_\mathrm{b} E^m_{y;\mathrm{scat}} - \varepsilon_\mathrm{b} \dfrac{\partial E^m_{y;\mathrm{scat}}}{\partial t} + \displaystyle\sum_i H^d_{x;\mathrm{scat}}(x_i, z_i, t)\delta(x - x_i)\delta(z - z_i) \\ -\dfrac{\partial E^m_{y;\mathrm{scat}}}{\partial x} = \mu_0 \dfrac{\partial H^m_{z;\mathrm{scat}}}{\partial t} \end{cases} \tag{47}$$

However, when the measurement scattered fields are treated *as time-dependent boundary conditions* (*BC's*), the adjoint Maxwell's equations become:

$$\begin{cases} \dfrac{\partial E^m_{y;\mathrm{scat}}}{\partial z} = \mu_0 \dfrac{\partial H^m_{x;\mathrm{scat}}}{\partial t} \\ -\dfrac{\partial H^m_{x;\mathrm{scat}}}{\partial z} + \dfrac{\partial H^m_{z;\mathrm{scat}}}{\partial x} = \sigma_\mathrm{b} E^m_{y;\mathrm{scat}} - \varepsilon_\mathrm{b} \dfrac{\partial E^m_{y;\mathrm{scat}}}{\partial t} \\ -\dfrac{\partial E^m_{y;\mathrm{scat}}}{\partial x} = \mu_0 \dfrac{\partial H^m_{z;\mathrm{scat}}}{\partial t} \end{cases} \tag{48}$$

$$\text{BC's}: \begin{cases} E^m_{y;\mathrm{scat}}(x_i, z_i, t) = E^d_{y;\mathrm{scat}}(x_i, z_i, t) \\ H^m_{x;\mathrm{scat}}(x_i, z_i, t) = H^d_{x;\mathrm{scat}}(x_i, z_i, t) \end{cases} \quad (x_i, z_i) \in \text{Observation line}; t = T \cdots 0$$

Now, a reinforced concrete slab (depth: 5 cm) with three square rebars having 0.707 cm sides and center locations (1, 2.5), (5, 2.5), and (9, 2.5) cm is considered as the host structure. Fig. 1 illustrates the cross-section of the damaged structure having a horizontal crack (crack area: 1 cm × 0.2 cm) with the center at (2.05, 2.5) cm and a debonding between the middle rebar and concrete with the debonding thickness of 0.2 cm. It is assumed that above and below the slab is occupied by air and actuators and sensors are located on the upper surface of the concrete slab.

The time history of the current density (unit in Amperes) is considered to be a Hanning window modulated sinusoid:

$$f(t) = [H(t) - H(t - N_p/f_c)][1 - \cos(2\pi f_c t/N_p)]\sin(2\pi f_c t) \tag{49}$$

where $H(t)$ is Heaviside function, $N_p = 0.5$, and $f_c = 4.34$ GHz is the dominant (central) frequency. Considering relative dielectric constant and conductivity of the concrete to be $\varepsilon_r = 5.3$ and $\sigma = 0.05$ S/m, the central wavelength of the excitation signal inside the concrete is about 3 cm ($\lambda_c \cong c_0/(\sqrt{\varepsilon_r} f_c)$). Also, based on 3% of the maximum amplitude of the excitation signal spectrum, the maximum frequency and minimum

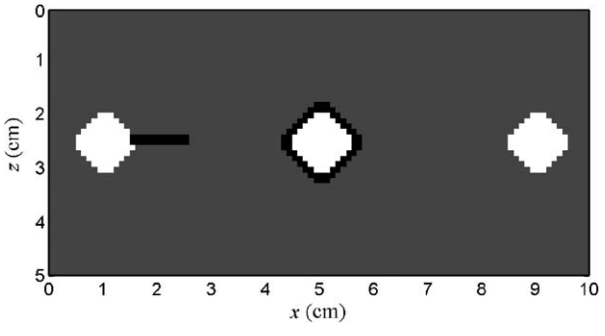

Fig. 1. Cross-section of a reinforced concrete slab with multiple damages.

wavelength of the signal in concrete are found to be about 19.5 GHz and 7 mm, respectively. It is also assumed that the properties of the rebars are $\varepsilon_r = 1$ and $\sigma = 1.03 \times 10^7$ S/m.

In this paper, a FDTD method based on *Yee algorithm* (Yee, 1966) with second–order of accuracy in both time and space is used for computation of all synthetic sensor data, incident field, and migration field. In order to avoid numerical dispersion and to ensure numerical stability, the FD grid sizes and the time step were chosen (Taflove, 1995): $\Delta x = \Delta z = 1$ mm and $\Delta t = 0.9\Delta x/(c_0\sqrt{2})$, where $c_0 = 3 \times 10^8$ m/s is the velocity of the EM waves in air.

The actuator and sensor spacings, Δ_a and the Δ_s, are important factors in image quality. A coarse actuator or sensor spacing will introduce spatial aliasing artifacts and lowers the dynamic range in the image (Chen and Schuster, 1999). In Kirchhoff migration, time-reversal, and diffraction tomography algorithms, for instance, the sensor spacing should not be more than one-half of the minimum wavelength of the signal in the structure, i.e. $\Delta_s = \lambda_{\min}/2$ (Schnieider, 1978; Alam et al., 2004; Kak and Slaney, 1988 and Weedon et al., 2000).

First, the imaging results of the EM migration in its prestack form with $\Delta_a = 10$ mm are presented. To show the effects of different measurement scenarios, sensor spacing, measurement noise, and discontinuity of the material properties of the host structure on the quality of the images, the following cases are investigated:

(A) $E^d_{y;\text{scat}}$ and $H^d_{x;\text{scat}}$ (as BC's; $\Delta_s = 7\text{ mm} = \lambda_{\min}$)
(B) $E^d_{y;\text{scat}}$ and $H^d_{x;\text{scat}}$ (as sources; $\Delta_s = 7\text{ mm} = \lambda_{\min}$)
(C) $E^d_{y;\text{scat}}$ (as BC's; $\Delta_s = 7\text{ mm} = \lambda_{\min}$)
(D) $H^d_{x;\text{scat}}$ (as BC's; $\Delta_s = 7\text{ mm} = \lambda_{\min}$)
(E) $E^d_{y;\text{scat}}$ and $H^d_{x;\text{scat}}$ (as BC's; $\Delta_s = 7\text{ mm} = \lambda_{\min}$; contaminated by noise with SNR = 5)
(F) $E^d_{y;\text{scat}}$ and $H^d_{x;\text{scat}}$ (as BC's; $\Delta_s = 7\text{ mm} = \lambda_{\min}$; model: half-space concrete slab without rebars and the same damages)
(G) $E^d_{y;\text{scat}}$ and $H^d_{x;\text{scat}}$ (as BC's; $\Delta_s = 5\text{ mm} \cong 0.7\lambda_{\min}$)
(H) $E^d_{y;\text{scat}}$ and $H^d_{x;\text{scat}}$ (as BC's; $\Delta_s = 10\text{ mm} \cong 1.4\lambda_{\min}$)

It should be mentioned that the conductivity and permittivity images with correlation imaging conditions are constructed from Eq. (45) and (46), respectively. Figs. 2–7 show the images obtained by the EM migration algorithm with different imaging conditions in case (A). Clearly, the conductivity images are superior to the permittivity ones. The geometries of the damages are correctly identified with the least artifacts in conductivity images shown in Figs. 3 and 5. Note that the actuator–sensor array can only reconstruct the upper part of the debonding due to the total reflection of EM waves by the metal rebar. Generally, the quality of the images based on the modified excitation-time imaging condition is better than that of the images based on the excitation-time imaging condition. From the conductivity images, it is also observed that the application of the maximum-energy travel time provides much better images compared to the images obtained by the first-arrival travel time. Note that the modified excitation-time imaging condition with maximum-energy travel time produces images comparable to the images obtained by the zero-lag cross-correlation imaging condition.

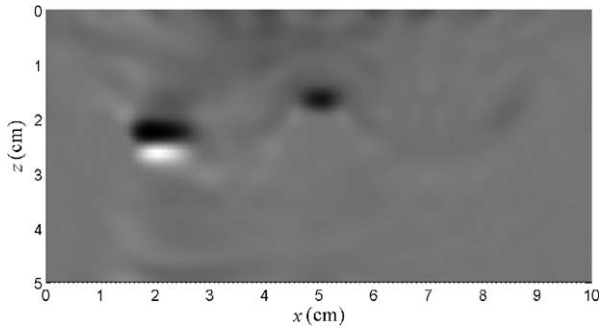

Fig. 2. Case (A): the permittivity image; zero-lag cross-correlation imaging condition.

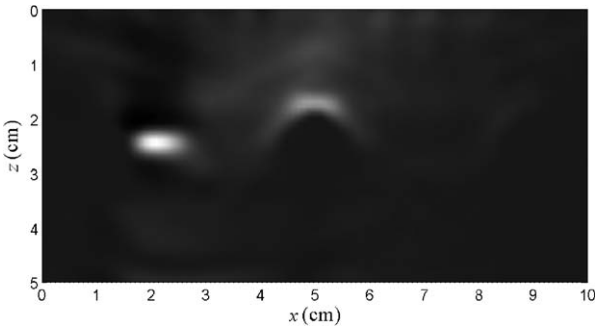

Fig. 3. Case (A): the conductivity image; zero-lag cross-correlation imaging condition.

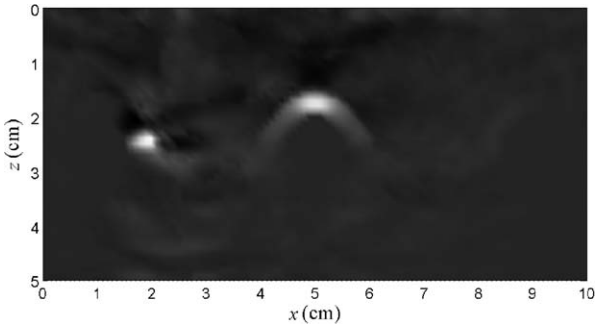

Fig. 4. Case (A): the conductivity image; excitation-time imaging condition (max-energy travel time).

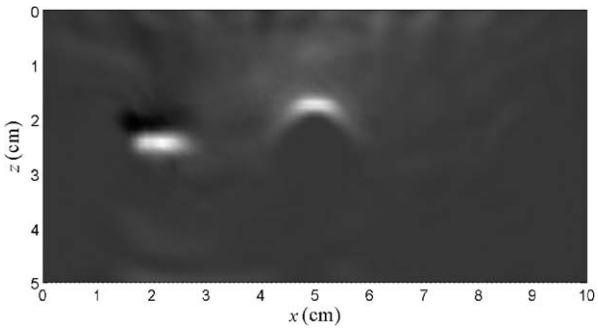

Fig. 5. Case (A): the conductivity image; modified excitation-time imaging condition (max-energy travel time).

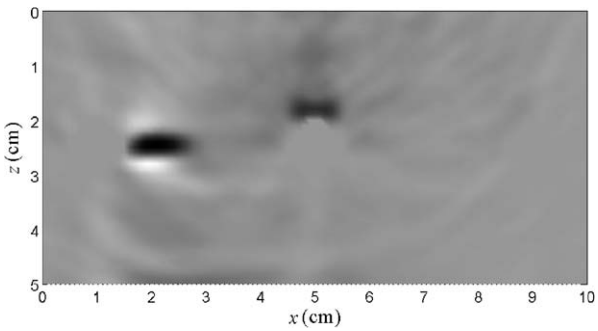

Fig. 6. Case (A): the conductivity image; excitation-time imaging condition (first-arrival travel time).

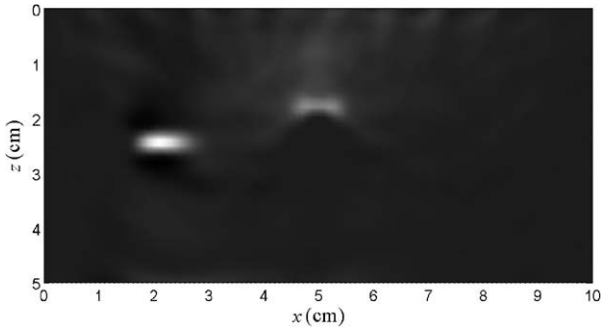

Fig. 7. Case (A): the conductivity image; modified excitation-time imaging condition (first-arrival travel time).

Due to space limitation, only some of the images in cases (B) to (H) are presented in the following. When the scattered data are treated as sources instead of time-dependent boundary conditions in EM migration, case (B), the quality of the images is deteriorated (by increasing the artifacts especially at sensor locations and not completely identifying the damage geometry). Note that unlike case (A), the permittivity images are superior in this case. Figs. 8 and 9 show permittivity images based on zero-lag cross correlation and modified excitation-time (with maximum-energy travel time) imaging conditions, respectively.

When only $E^d_{y;\mathrm{scat}}$ is used as BC's in the algorithm, case (C), the resulting images are very similar to those obtained using both $E^d_{y;\mathrm{scat}}$ and $H^d_{x;\mathrm{scat}}$. Figs. 10 and 11 illustrate conductivity images based on correlation and modified excitation-time (with maximum-energy travel time) imaging conditions, respectively. Figs. 12 and 13 also show two conductivity images when only $H^d_{x;\mathrm{scat}}$ is used in the algorithm, case (D).

To show the robustness of the imaging algorithm to measurement noise, each components of the measurement data, $E^d_{y;\mathrm{scat}}$ and $H^d_{x;\mathrm{scat}}$, are contaminated by an additive white Gaussian noise with zero mean and standard deviation σ (not confused with the conductivity). SNR is considered to be equal to 5 with the following definition for the $E^d_{y;\mathrm{scat}}$ component:

$$\mathrm{SNR} = 10\log_{10}\left\{\frac{\mathrm{Mean}\left[\left(E^d_{y;\mathrm{scat}}\right)^2\right]}{\sigma^2}\right\} \tag{50}$$

Figs. 14 and 15 show the measurement noise effect on two conductivity images in case (E).

It should be noted that the artifacts present in the images are due to several factors some of which are coarse actuator and sensor spacing, limited aperture of the measurement line, limited bandwidth of the excitation signal, and discontinuity in the material properties of the host structure. To realize the effect of the last factor, a new model including a half-space concrete without rebars and the same damages is considered. Figs. 16–21 illustrate some images in this case.

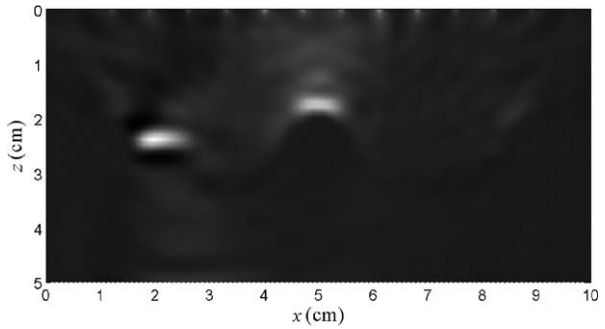

Fig. 8. Case (B): the permittivity image; zero-lag cross-correlation imaging condition.

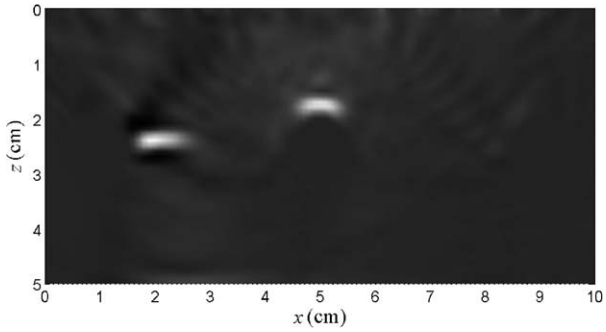

Fig. 9. Case (B): the permittivity image; modified excitation-time imaging condition (max-energy travel time).

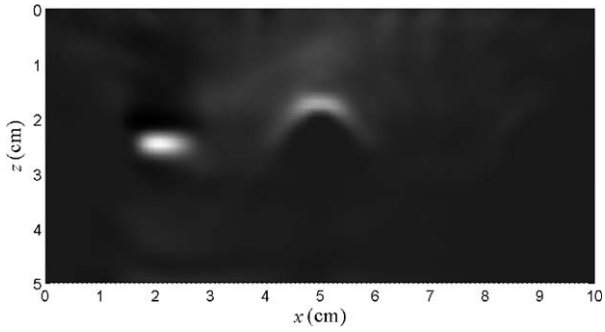

Fig. 10. Case (C): the conductivity image; zero-lag cross-correlation imaging condition.

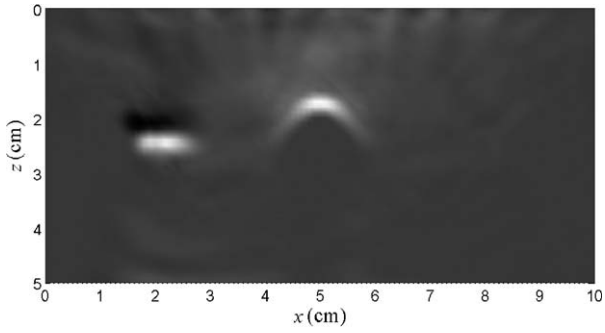

Fig. 11. Case (C): the conductivity image; modified excitation-time imaging condition (max-energy travel time).

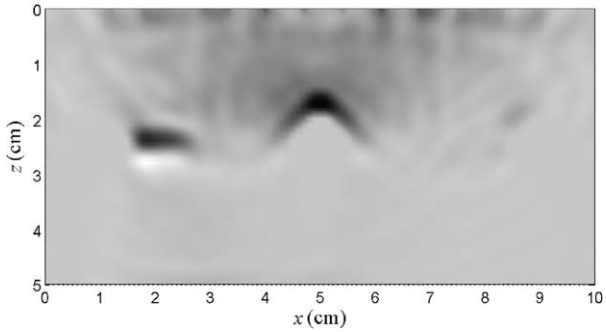

Fig. 12. Case (D): the conductivity image; zero-lag cross-correlation imaging condition.

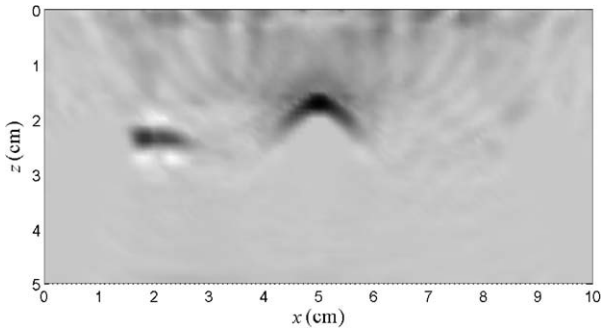

Fig. 13. Case (D): the conductivity image; modified excitation-time imaging condition (max-energy travel time).

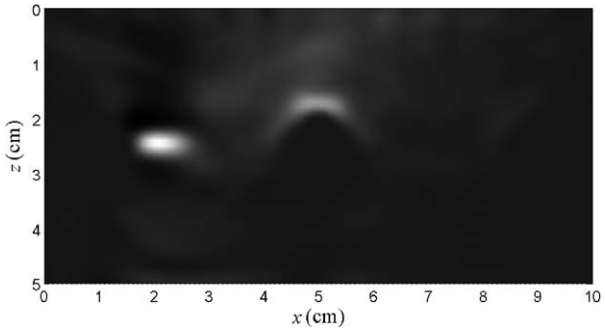

Fig. 14. Case (E): the conductivity image; zero-lag cross-correlation imaging condition; Noisy data SNR = 5.

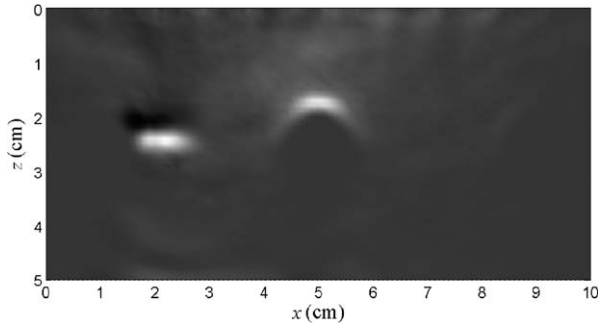

Fig. 15. Case (E): the conductivity image; modified excitation-time imaging condition (max-energy travel time); Noisy data SNR = 5.

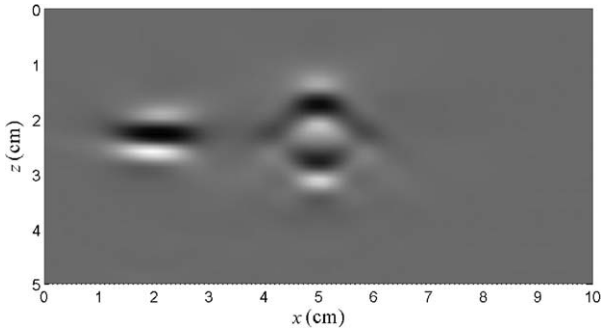

Fig. 16. Case (F): the permittivity image; zero-lag cross-correlation imaging condition; Half-space concrete.

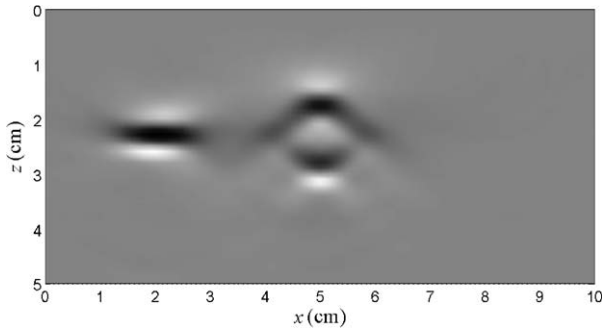

Fig. 17. Case (F): the permittivity image; modified excitation-time imaging condition (max-energy travel time); Half-space concrete.

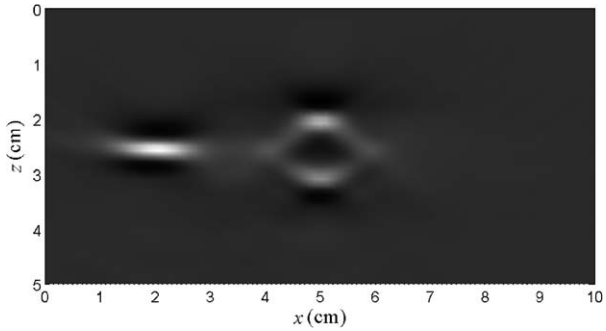

Fig. 18. Case (F): the permittivity image; modified excitation-time imaging condition (first-arrival travel time); Half-space concrete.

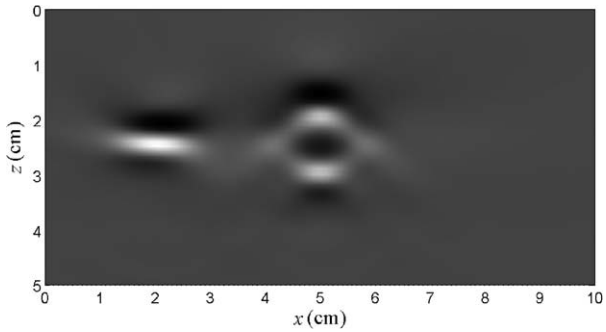

Fig. 19. Case (F): the conductivity image; zero-lag cross-correlation imaging condition; Half-space concrete.

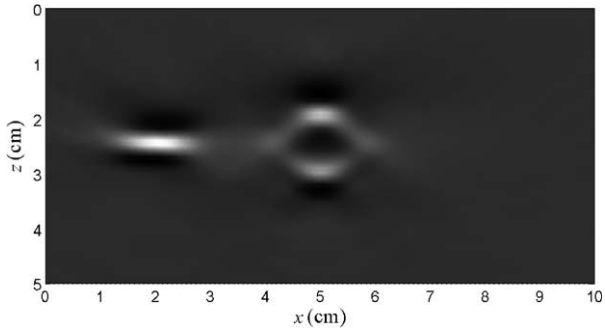

Fig. 20. Case (F): the conductivity image; modified excitation-time imaging condition (max-energy travel time); Half-space concrete.

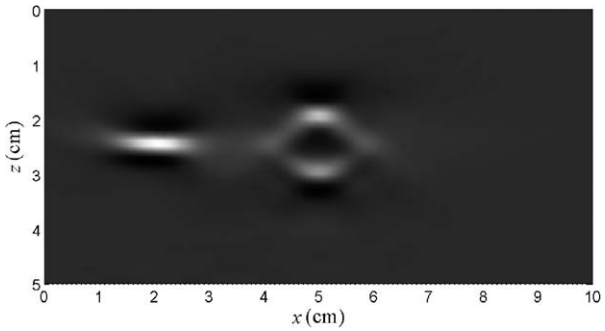

Fig. 21. Case (F): the conductivity image; modified excitation-time imaging condition (first-arrival travel time); Half-space concrete.

It is observed that both permittivity and conductivity images provide similar damage identification in this case. Moreover, the quality of the images based on the first and maximum-energy arrivals becomes very close due to this simple host structure. Notice how some artifacts in case (A), especially the ones near the interfaces, disappear on the corresponding images in case (F).

In order to show the effect of the sensor spacing on the images quality, the images with three different spacing values, $\Delta_s = 0.7\lambda_{\min}, \lambda_{\min}, 1.4\lambda_{\min}$, are compared. Figs. 22–24 show the conductivity images based on the modified excitation-time imaging condition and maximum-energy arrival for different sensor spacings. The artifacts due to the coarse sensor spacing can be easily observed in Fig. 24 with $\Delta_s = 1.4\lambda_{\min}$.

Now, let us perform the poststack form of the EM migration. To this end, zero-time imaging condition is applied to the migration scattered field components ($E^m_{y;\text{scat}}, H^m_{x;\text{scat}},$ and $H^m_{z;\text{scat}}$) computed in a 2:1 scaled host structure model. Therefore, three different images can be obtained. As previously mentioned, the measurement

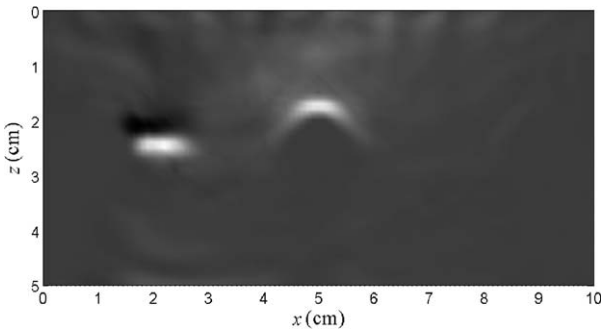

Fig. 22. Case (G): the conductivity image; modified excitation-time imaging condition (max-energy travel time); $\Delta_s = 0.7\lambda_{\min}$.

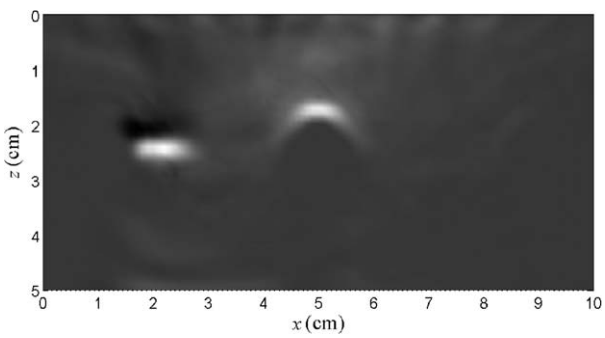

Fig. 23. Case (A): the conductivity image; modified excitation-time imaging condition (max-energy travel time); $\Delta_s = \lambda_{\min}$.

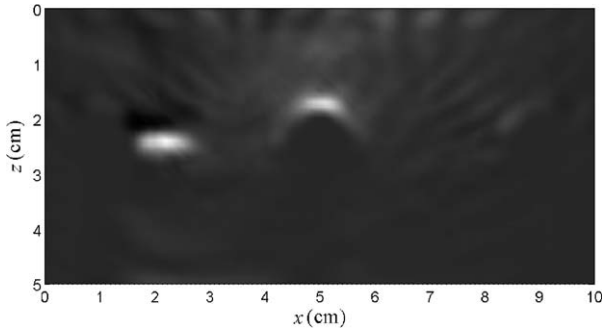

Fig. 24. Case (H): the conductivity image; modified excitation-time imaging condition (max-energy travel time); $\Delta_s = 1.4\lambda_{\min}$.

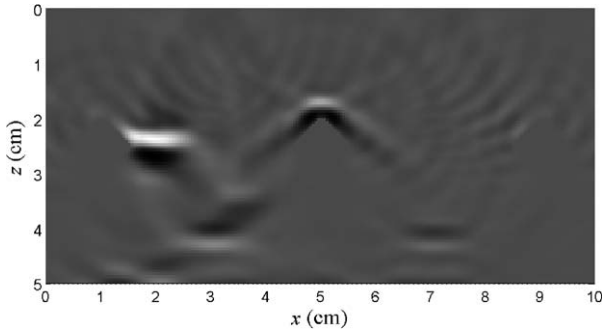

Fig. 25. The $E^m_{y;\text{scat}}$-image obtained by poststack EM migration; 26 actuator/sensor pairs.

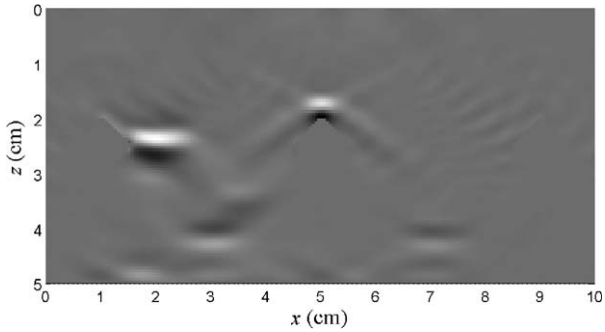

Fig. 26. The $H^m_{x;\text{scat}}$-image obtained by poststack EM migration; 26 actuator/sensor pairs.

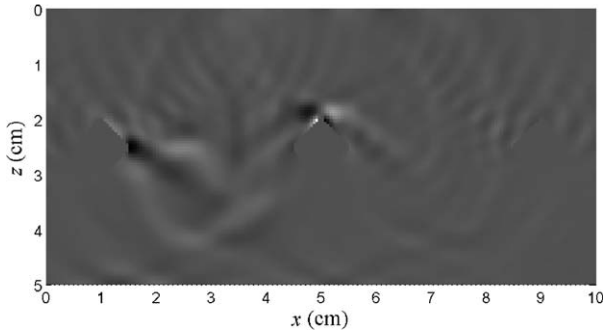

Fig. 27. The $H^m_{z;\text{scat}}$-image obtained by poststack EM migration; 26 actuator/sensor pairs.

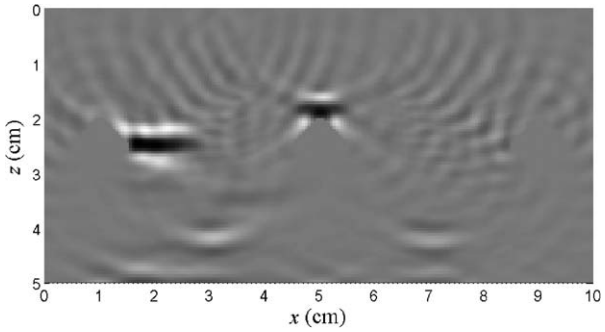

Fig. 28. The $E^m_{y;\mathrm{scat}}$-image obtained by poststack EM migration; 26 actuator/sensor pairs.

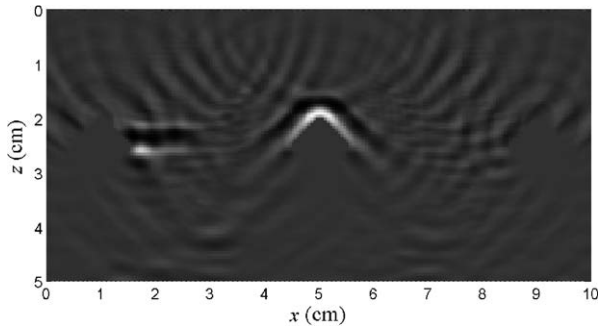

Fig. 29. The $E^m_{y;\mathrm{scat}}$-image obtained by poststack EM migration; 26 actuator/sensor pairs.

data must be collected in a zero-offset experiment. It should be noted that the synthetic data produced based on the exploding reflector model does not represent the zero-offset data. Therefore, instead of solving the forward problem one time using exploding reflector model, the problem should be solved as many times as the number of sensor/actuator pairs using the actual damaged model to obtain the synthetic data. It is worth mentioning that Sanada and Ashida (1998) applied a 2-D TM poststack reverse-time migration using FDTD method. However, the synthetic sensor data was calculated based on incorrect exploding reflector model.

The resulting images using the data collected by eleven sensor/actuator pairs ($\Delta_s = \Delta_a = 1$ cm), not shown here, had a lot of strong artifacts such that the damages could not be identified. The following images are obtained with twenty six sensor/actuator pairs ($\Delta_s = \Delta_a = 0.4$ cm). Figs. 25–27 present three resulting images when both $E^d_{y;\mathrm{scat}}$ and $H^d_{x;\mathrm{scat}}$ are used as BC's in the algorithm.

The best image, $E^m_{y;\mathrm{scat}}$-image, when $E^d_{y;\mathrm{scat}}$ and $H^d_{x;\mathrm{scat}}$ are used as sources in the algorithm is shown in Fig. 28.

The images when only $E^d_{y;\mathrm{scat}}$ is used as BC's are very similar to Figs. 25–27. Finally, the best image when only $H^d_{x;\mathrm{scat}}$ is used as BC's is displayed in Fig. 29.

In view of the poststack images, it is observed that $E^m_{y;\mathrm{scat}}$-images provide the highest resolution. However, even with 26 collocated actuator/sensor pairs, the quality of the $E^m_{y;\mathrm{scat}}$-images are lower than the prestack images quality.

6. Conclusions

Knowing that identifying geometries of damages with fast algorithms is the primary and minimum goal of a SHMS, EM migration has been adopted to image different damages in reinforced concrete structures. This algorithm has been formulated in time-domain for 3-D inhomogeneous isotropic and lossy structures. To speed up the imaging process, the application of different excitation-time imaging conditions instead of applying zero-lag cross-correlation imaging condition has been examined. Moreover, the images based on the

poststack concept have been compared to the prestack images. To show the effectiveness of the imaging algorithm, numerical simulations in 2-D TM case for a reinforced concrete slab with multiple damages have been performed. All synthetic sensor data, incident field, and migration field have been computed via a FDTD method with second–order of accuracy in time and space.

Considering the resulting images, the following conclusions may be drawn:

- The EM migration algorithm is able to correctly identify the damages geometries.
- The algorithm is quite robust against measurement noise.
- When the scattered data are used as sources instead of time-dependent boundary conditions in EM migration, the quality of the images is deteriorated.
- The application of the modified excitation-time imaging condition with maximum-energy travel time produces images with quality close to those produced by zero-lag cross correlation imaging condition. Thus, the application of the modified imaging condition to the imaging algorithm significantly reduces the computational cost without losing the image quality.
- Although in the 2-D EM migration algorithm both $E^d_{y;\mathrm{scat}}$ and $H^d_{x;\mathrm{scat}}$ appear in the formulation, a complete image still may be constructed using one of these components.
- If any discontinuity in material properties exists in the host (healthy) structure model, some artifacts may occur in the resulting image.

Examining the poststack images, it is observed that the quality of the images is lower than those in the prestack form, as expected. However, the poststack concept may be employed when a rough but fast damage identification is required.

To further reduce the computational cost of the algorithm, solving the integral equations representing the migration scattered wavefield with pre-computed Green's functions instead of solving the differential equations using FDTD method need to be investigated.

Acknowledgement

This research was supported by the National Science Foundation under Grant CMS-0301441. Mr. Nojavan would like to acknowledge support by a fellowship from Goodrich Corporation.

References

Alam, M., McClellan, J.H., Norville, P., Scott, W.R., 2004. Time-reverse imaging for detection of landmines. In: Harmon, R.S., Broach, J.T., Holloway, J.H. (Eds.), Proceedings of SPIE, Detection and Remediation Technologies for Mines and Minelike Targets IX, 5415, pp. 167–174.

Audebert, F., Nichols, D., Rekdal, T., Biondi, B., Lumley, D., Urdaneta, H., 1997. Imaging complex geologic structure with single-arrival Kirchhoff prestack depth migration. Geophysics 62 (5), 1533–1543.

Bahr, A.J., 1995. Experimental techniques in microwave NDE. Review of Progress in Quantitative Nondestructive Evaluation 14, 593–600.

Biondi, B.L., 2004. 3-D Seismic Imaging. Stanford University.

Bray, D.E., McBride, D., 1992. Nondestructive Testing Techniques. John Wiley & Sons Inc., New York.

Buyukozturk, O., 1998. Imaging of concrete structures. NDT&E International 31 (4), 233–243.

Chang, F.K., 1997. Structural health monitoring: a summary report. In: First International Workshop on Structural Health Monitoring, Stanford University, September 18–20, 1997, pp. xix–xxix.

Chang, W.F., McMechan, G.A., 1986. Reverse time migration of offset vertical seismic profiling data using the excitation time imaging condition. Geophysics 51 (1), 67–84.

Chang, W.F., McMechan, G.A., 1994. 3-D elastic prestack reverse time depth migration. Geophysics 59 (4), 597–609.

Chaturvedi, P., Plumb, R.G., 1995. Electromagnetic imaging of underground targets using constrained optimization. IEEE Transactions on Geoscience and Remote Sensing 33 (3), 551–561.

Chen, H.W., Huang, T.M., 1998. Finite-difference time-domain simulation of GPR data. Journal of Applied Geophysics 40, 139–163.

Chen, J., Schuster, G.T., 1999. Resolution limits of migrated images. Geophysics 64, 1046–1053.

Claerbout, J.F., 1971. Toward a unified theory of reflector mapping. Geophysics 36 (3), 467–481.

Claerbout, J.F., Black, J.L., 2001. Basic Earth Imaging. © December 7, 2001, Version 2.4.

Cui, T.J., Chew, W.C., 2002. Diffraction tomographic algorithm for the detection of 3D objects buried in a lossy half-space. IEEE Transaction on Antennas and Propagation 50 (1), 42–49.

Felsen, L., Marcuvitz, N., 1994. Radiation and Scattering of Waves. IEEE Press, New York.

Gray, S.H., 1999. Speed and accuracy of seismic migration methods. In: Lines, L.R., Lawton, D.C., Gray, S.H. (Eds.), Depth Imaging of Foothills Seismic Data.

Hadamard, J., 1923. Lectures on the Cauchy Problem in Linear Partial Differential Equations. Yale University Press.

Haykin, S., 1999. Neural Networks, A Comprehensive Foundation, Second ed. Prentice Hall, New Jersey.

Iyer, S.R., Sinha, S.K., Schokker, A.J., 2005. Ultrasonic C-scan imaging of post-tensioned concrete bridge structures for detection of corrosion and voids. Computer-Aided Civil and Infrastructure Engineering 20, 79–94.

Johansson, E.M., Mast, J.E., 1994. Three dimensional ground penetration radar imaging using synthetic aperture time-domain focusing. In: Proceedings SPIE, vol. 2275, July 25–26, 1994, pp. 205–214.

Kak, A.C., Slaney, M., 1988. Principles of Computerized Tomographic Imaging. IEEE Press.

Kim, Y.J., Jofre, L., Flaviis, F.D., Feng, M.Q., 2004. Microwave subsurface imaging technology for damage detection. Journal of Engineering Mechanics 130 (7), 858–866.

Kosmas, P., Rappaport, C.M., 2005. Time reversal with the FDTD method for microwave breast cancer detection. IEEE Transactions on Microwave Theory and Techniques 53 (7), 2317–2323.

Krautkramer, J., Krautkramer, H., 1990. Ultrasonic Testing of Materials. Springer-Verlag, Berlin.

Lemistre, M.B., Balageas, D.L., 2004. A hybrid electromagnetic acousto-ultrasonic method for SHM of carbon/epoxy structures. Structural Health Monitoring 2 (2), 153–160.

Lin, X., Yuan, F.G., 2001. Detection of multiple damages by prestack reverse-time migration technique. AIAA Journal 39 (11), 2206–2215.

Lin, X., Yuan, F.G., in press. Experimental study of applying migration technique in structural health monitoring. International Journal of Structural Health Monitoring.

Liu, J., Bethesda, W., 1998. Microwave and ultrasonic NDE of thick glass-fiber-reinforcement composites. In: Proceedings of SPIE on NDE on materials and composites II, vol. 3396, pp. 135–146.

Loewenthal, D., Hu, L.Z., 1991. Two methods for computing the imaging condition for common-shot prestack migration. Geophysics 56 (3), 378–381.

Marklein, R., Mayer, K., Hannemann, R., Kraylow, T., Balasubramanian, K., Langenberg, K.J., Schmitz, V., 2002. Linear and nonlinear inversion algorithms applied in nondestructive evaluation. Inverse Problems 18, 1733–1759.

Pastorino, M., Caorsi, S., Massa, A., 2002. A global optimization technique for microwave nondestructive evaluation. IEEE Transactions on Instrumentation and Measurement 51 (4), 666–673.

Rekanos, I.T., Raisanen, A., 2003. Microwave imaging in the time domain of buried multiple scatterers by using an FTDT-based optimization technique. IEEE Transactions on Magnetics 39 (3), 1381–1384.

Sabbagh, H.A., Sabbagh, L.D., Roberts, T.M., 1988. An eddy current model and algorithm for three dimensional nondestructive evaluations of advanced composites. IEEE Transactions on Magnetics 24 (6), 3201–3212.

Sanada, Y., Ashida, Y., 1998. Reverse time migration for ground penetration radar using finite difference time domain method. In: Proceedings of the 3rd International Symposium on Recent advances in Exploration Geophysics, Kyoto, pp. 145–154.

Scales, J.A., 1997. Theory of Seismic Imaging. Samizdat Press, Golden, White River Junction.

Schnieider, W.A., 1978. Integral formulation for migration in two and three dimensions. Geophysics 43 (1), 49–76.

Slaney, M., Kak, A.C., Larsen, L.E., 1984. Limitation of imaging with first-order diffraction tomography. IEEE Transactions on Microwave and Techniques 32 (8), 860–874.

Taflove, A., 1995. Computational Electrodynamics: the Finite Difference Time Domain Method. Artech House, Boston.

Van den Berg, P.M., Kleinman, R.E., 1997. A contrast source inversion method. Inverse Problems 13, 1607–1620.

Vidale, J.E., 1988. Finite difference travel time calculation. Bulletin of the Seismological Society of America 78, 2062–2076.

Wang, L., Yuan, F.G., 2005. Damage identification in a composite plate using prestack reverse-time migration technique. Structural Health Monitoring 4 (3), 195–211.

Wang, T., Oristaglio, M., Tripp, A., Hohmann, G., 1994. Inversion of diffusive transient electromagnetic data by a conjugate gradient method. Radio Science 29 (4), 1143–1156.

Weedon, W.H., Chew, W.C., Mayes P.E., 2000. A step-frequency radar imaging system for microwave nondestructive evaluation. Progress in Electromagnetics Research, PIER 28, 121–146.

Yavuz, M.E., Teixeira, F.L., 2005. A numerical study of time-reversed UWB electromagnetic waves in continuous random media. IEEE Antennas and Wireless Propagation Letters 4, 43–46.

Yee, K.S., 1966. Numerical solution of initial boundary value problems involving Maxwell's equations in isotropic media. IEEE Transactions on Antennas and Propagation 14, 302–307.

Zhdanov, M.S., 1988. Integral Transforms in Geophysics. Springer-Verlag, Berlin.

Zhdanov, M.S., 2001. Method of broad band electromagnetic holographic imaging: US Patent # 6,253,100.

Zhdanov, M.S., 2002. Geophysical Inverse Theory and Regularization Problems. Elsevier Science, Amsterdam, Oxford.

Zhdanov, M.S., Portniaguine, O., 1997. Time domain electromagnetic migration in the solution of inverse problem. Geophysics J. Int. 131, 293–309.

Zhu, J., Lines, L.R., 1997. Implicit interpolation in reverse time migration. Geophysics 62, 906–917.

Zoghi, R., 2000. Microwave Non-Destructive Testing and Evaluation. Kluwer Academic Publishers.